

Elliptic Flow in Heavy-Ion Collisions at Energies $\sqrt{s_{NN}} = 2.7\text{--}39$ GeV

Yu. B. Ivanov^{1,2,*} and A. A. Soldatov^{2,†}

¹*National Research Centre "Kurchatov Institute" (NRC "Kurchatov Institute"), Moscow 123182, Russia*

²*National Research Nuclear University "MEPhI" (Moscow Engineering Physics Institute), Moscow 115409, Russia*

The transverse-momentum integrated elliptic flow of charged particles at midrapidity, $v_2(\text{charged})$, and that of identified hadrons from Au+Au collisions are computed in a wide range of incident energies $2.7 \text{ GeV} \leq \sqrt{s_{NN}} \leq 39 \text{ GeV}$. The simulations are performed within a three-fluid model employing three different equations of state (EoS's): a purely hadronic EoS and two versions of the EoS involving the deconfinement transition—a first-order phase transition and a smooth crossover one. The present simulations demonstrate low sensitivity of $v_2(\text{charged})$ to the EoS. All considered scenarios equally well reproduce recent STAR data on $v_2(\text{charged})$ for mid-central Au+Au collisions and properly describe its change of sign at the incident energy decrease below $\sqrt{s_{NN}} \approx 3.5 \text{ GeV}$. The predicted integrated elliptic flow of various species exhibits a stronger dependence on the EoS. A noticeable sensitivity to the EoS is found for anti-baryons and, to a lesser extent, for K^- mesons. In particular, the v_2 excitation functions of anti-baryons exhibit a non-monotonicity within the deconfinement scenarios that was predicted by Kolb, Sollfrank and Heinz. However, low multiplicities of anti-baryons at $\sqrt{s_{NN}} \leq 10 \text{ GeV}$ result in large fluctuations of their v_2 which may wash out this non-monotonicity.

PACS numbers: 25.75.-q, 25.75.Nq, 24.10.Nz

Keywords: relativistic heavy-ion collisions, elliptic flow, hydrodynamics, deconfinement

I. INTRODUCTION

The Beam Energy Scan (BES) program at the Relativistic Heavy Ion Collider (RHIC) at Brookhaven National Laboratory (BNL) pursues the major goal of exploring the QCD phase diagram of the strongly interacting matter. The main questions addressed in this research are: At which energy does onset of deconfinement happen? What is the order of the deconfinement transition at high baryon densities? Is there a critical end point in the phase diagram? The BES program at RHIC provides us with a unique opportunity to study systematically the collision energy dependence of a large number of observables. The present study is inspired by recent papers of the STAR Collaboration [1, 2] on the beam-energy dependence of the elliptic flow (v_2) in the BES region.

The beam-energy dependence of the collective flow has been recently studied within several different models [3–13] with the main emphasis on search of signals of the onset of deconfinement. A non-monotonicity of the transverse-momentum integrated (p_t -integrated) v_2 was predicted in Ref. [3] which is related to the quark-hadron phase transition and the corresponding softening of the EoS in the transition region. However, later it was stated [4] that in the experimental data this phase transition signature will be washed out by strong viscous effects in the late hadronic phase, where the fireball spends most of its time. As a result, the experimentally measured integrated elliptic flow v_2 should rise monotonically with

the center-of-mass energy, $\sqrt{s_{NN}}$, approaching the ideal fluid limit only at or above RHIC energies.

On the other hand, in Ref. [14] it was found that the hadron resonance gas with a large baryon density is closer to the ideal fluid limit than the corresponding gas with zero baryon density. Moreover, a nonzero baryon chemical potential serves not only to reduce the effect of dissipative terms of the first order in gradients but also of the second-order terms. This effect of the baryon chemical potential was noticed even earlier in Ref. [15]. The latter suggests that the system created at lower collision energies may display a fluid-like behavior with an effective fluidity close to that found at RHIC top-energy collisions, thus explaining why the differential elliptic flow measured at lower RHIC energies is close to that observed at the top RHIC energies. Indeed, an effective fluidity extracted from experimental data on collective flow [16] indicates that the viscosity at lower BES-RHIC energies is only slightly higher than that at the top RHIC energy. Above findings were supported by actual simulations within a hybrid model [5]. It was found that the triangular flow provides the clearer signal for the formation of low-viscous fluid in heavy ion collisions. Moreover, the kinetic phase produces additional elliptic flow rather than destroy it which also testify in favor of low-viscous fluid at low BES energies.

At the same time in Ref. [6] it was pointed out a strong influence of initial conditions for the hydrodynamic evolution on the observed v_2 values, thus questioning the standard interpretation that the hydrodynamic limit is only reached at RHIC energies. The integrated and differential elliptic flow for charged particles at SPS energies was found to be mostly sensitive to viscosity rather than to the EoS [7]. Recently, a low sensitivity of the elliptic flow to the type of the phase transition (or its absence)

*e-mail: Y.Ivanov@gsi.de

†e-mail: saa@ru.net

in the EoS was already reported [17] at RHIC energies. Thus, the situation is somewhat controversial and needs further investigation.

In the present paper we report results on the collision energy dependence of the midrapidity transverse-momentum integrated elliptic flow of charged particles and that of identified hadrons produced in Au+Au collisions using a model of the three-fluid dynamics (3FD) [18] employing three different equations of state (EoS): a purely hadronic EoS [19] (hadr. EoS) that was used in calculations of the collective flow so far [20–22] and two versions of EoS involving the deconfinement transition [24]. These two versions are an EoS with the first-order phase transition (2-phase EoS) and that with a smooth crossover transition (crossover EoS). We report results of simulations in the energy range from 2.7 GeV to 39 GeV in terms of $\sqrt{s_{NN}}$. This domain goes beyond the range of the RHIC BES program and also covers energies of the Alternating Gradient Synchrotron (AGS) at BNL and the Super Proton Synchrotron (SPS) of the European Organization for Nuclear Research (CERN). The reported results are also relevant to newly constructed Facility for Antiproton and Ion Research (FAIR) in Darmstadt and the Nuclotron-based Ion Collider Facility (NICA) in Dubna.

The 3FD model does not include viscosity in its formulation. However, dissipation is present in the 3FD through friction interaction between participated fluids. It would be interesting to estimate this dissipation in terms of viscosity of the conventional 1-fluid hydrodynamics. This work is in progress. Numerical solution of the model is performed in (3+1) dimensions on spacial grid with a finite cell size. The numerical scheme (the particle-in-cell method) has a relatively small numerical viscosity, which is comparable to the minimal viscosity that occurs at deconfinement transition [23]¹. Details of these calculations are described in Ref. [25] dedicated to analysis of the baryon stopping.

We would like to mention explicitly that no tuning (or change) of 3FD-model parameters or parameters of the used EoS's has been performed in this study as compared to previous simulations [12, 25–29] in which various bulk observables were considered precisely in the same range of incident energies. The main goal of this series of works [12, 25–29] is to analyze a whole set of various observables within the same description without any observable-dependent tuning of the parameters. It enables us to reveal possible correlations in excitation functions of various observables within different scenarios, which can be used as experimental indications of the deconfinement onset or its absence.

II. THE 3FD MODEL

A three-fluid approximation is a minimal way to simulate a finite stopping power of colliding nuclei at high incident energies. Within this approximation a generally nonequilibrium distribution of baryon-rich matter is modeled by counter-streaming baryon-rich fluids initially associated with constituent nucleons of the projectile (p) and target (t) nuclei. In addition, newly produced particles, populating the midrapidity region, are associated with a separate net-baryon-free fluid which is called a “fireball” fluid (f-fluid), following the Frankfurt group [30, 31]. A certain formation time τ is allowed for the f-fluid, during which the matter of the fluid propagates without interactions. The formation time is associated with a finite time of string formation. It is similarly incorporated in kinetic transport models such as the Ultra-relativistic Quantum Molecular Dynamics (UrQMD) [32], the Hadron string Dynamics (HSD) [33] and the Parton-Hadron String Dynamics (PHSD) [34]. Each of these fluids (the f-fluid after its formation) is governed by conventional hydrodynamic equations which contain interaction terms in their right-hand sides. These interaction terms describe mutual friction of the fluids and production of the f-fluid. The friction between fluids was fitted to reproduce the stopping power observed in proton rapidity distributions for each EoS, as it is described in Ref. [25] in detail. The main difference concerning the f-fluid in considered alternative scenarios consists in different formation times: $\tau = 2$ fm/c for the hadronic scenario and $\tau = 0.17$ fm/c for scenarios involving the deconfinement transition [25]. Large formation time within the hadronic scenario was chosen in order to reproduce mesonic yields at SPS energies. This was done in line with a principle of fair treatment of any EoS: any possible uncertainties in the parameters are treated in favor of the EoS, i.e. for each EoS the dynamical parameters of the model are chosen (within their uncertainty range) in such a way that the best possible reproduction of observables is achieved with this EoS.

Since each fluid is governed by its own hydrodynamic equations, it is locally characterized by its own set of hydrodynamic quantities—baryon and energy densities, velocities and, in particular, temperature and baryon chemical potential—which, in general, differ from those of other fluids. At the same time, all three fluids are described by the same EoS (chosen for the simulation), of course, with the pressure and energy density taken at their specific values of the temperature and baryon chemical potential. At the initial stage of the reaction all three fluids coexist in the same space-time region, thus describing a certain *nonequilibrium* state of the matter. It may happen that one or two of the fluids occur in the quark-gluon phase while other(s) is(are) in the hadronic one. This is a kind of a nonequilibrium mixed phase that is also possible in the model.

At the final stage of the collision the p- and t-fluids are either spatially separated or unified, while the f-fluid

¹ We use the same numerical scheme as that in Ref. [23].

still overlaps with the baryon-rich (p- and t-) fluids to a lesser (at high energies) or greater (at lower energies) extent. The freeze-out is performed accordingly to the procedure described in Ref. [18] and in more detail in Refs. [35, 36]. The freeze-out criterion is based on a local energy density, ε_{tot} , defined as a sum of contributions from all (p-, t- and f-) fluids being present in a local space-time region. The freeze-out procedure starts if $\varepsilon_{\text{tot}} < \varepsilon_{\text{frz}}$. The freeze-out energy density $\varepsilon_{\text{frz}} = 0.4 \text{ GeV/fm}^3$ was chosen mostly on the condition of the best reproduction of secondary particle yields. To the moment of the freeze-out the matter is already in the hadronic phase in the case of the 2-phase EoS, while for the crossover EoS this is not so. However, this is not a problem because, any case, the thermodynamic quantities of the frozen-out matter are recalculated from the in-matter EoS, with which the hydrodynamic calculation runs, to the hadronic gas EoS². This is done because a part of the energy is still accumulated in collective mean fields at the freeze-out instant. This mean-field energy should be released before calculating observables. Otherwise, the energy conservation would be violated. The freeze-out is performed locally (in a local spatial cell meeting the freeze-out condition), simultaneously for all fluids populating this cell. Thus, the freeze-out configuration of the matter is generally nonequilibrium.

Figure 1 illustrates the EoS's used in the simulations and the onset of the deconfinement transition in mid-central Au+Au collisions. Similarly to Ref. [37], the figure displays dynamical trajectories of the matter in the central box placed around the origin $\mathbf{r} = (0, 0, 0)$ in the frame of equal velocities of colliding nuclei. Initially, the colliding nuclei are placed symmetrically with respect to the origin $\mathbf{r} = (0, 0, 0)$ along z axis which is the direction of the beam. At a given density n_B , the energy density ε cannot be lower than the zero-temperature compressional energy, $\varepsilon(n_B, T = 0)$, so the accessible region is correspondingly limited. In the case of the crossover EoS only the region of the mixed phase between the QGP fraction $W_{\text{QGP}} = 0.1$ and $W_{\text{QGP}} = 0.5$ is displayed, because in fact the mixed phase occupies the whole $(\varepsilon - n_B)$ region. The $\varepsilon - n_B$ representation is chosen because these quantities are suitable to compare calculations with different EoS's. Only expansion stages of the dynamical trajectories are displayed, because the matter in the box is close to thermalization then. The criterion of the thermalization³ is the equality of longitudinal and transverse pressures in the box with an accuracy better than 10%. These pressures are calculated by means of summation of the corresponding diagonal elements of the hydrodynam-

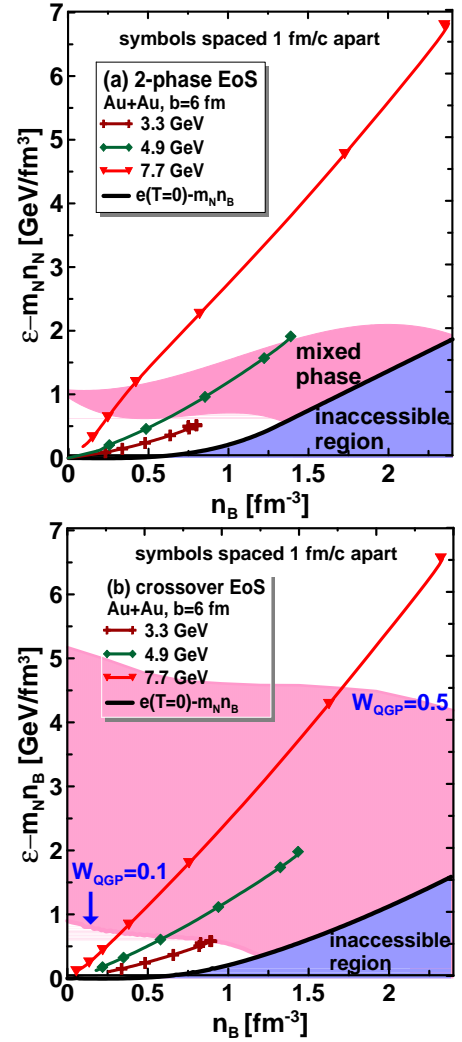


FIG. 1: (Color online) Dynamical trajectories of the matter in a central box of the colliding nuclei ($4\text{fm} \times 4\text{fm} \times \gamma_{cm} 4\text{fm}$), where γ_{cm} is the Lorentz factor associated with the initial nuclear motion in the c.m. frame, for mid-central ($b = 6 \text{ fm}$) Au+Au collisions at $\sqrt{s_{NN}} = 3.3, 4.9$ and 7.7 GeV . The trajectories are plotted in terms of the baryon density (n_B) and the energy density minus n_B multiplied by the nucleon mass ($\varepsilon - m_N n_B$). Only expansion stages of the matter evolution are displayed. Symbols on the trajectories indicate the time rate of the evolution: time span between marks is 1 fm/c . For the 2-phase EoS (a) the shadowed “mixed phase” region is located between the borders, where the QGP phase starts to raise ($W_{\text{QGP}} = 0$) and becomes completely formed ($W_{\text{QGP}} = 1$). For the crossover EoS (b) the displayed borders correspond to values of the QGP fraction $W_{\text{QGP}} = 0.1$ and 0.5 . Inaccessible region is restricted by $\varepsilon(n_B, T = 0) - m_N n_B$ from above.

² In this gas EoS, as well as in the hadr. EoS, 48 different hadronic species are taken into account. Each hadronic species includes all the relevant isospin states, e.g., the nucleon species includes proton and neutron.

³ strictly speaking, a randomization of the initial momentum because the matter is still chemically nonequilibrium

ical energy-momentum tensor T_{ii}^α of ($i = p, t, f$)-fluids in the c.m. frame of colliding nuclei

$$P_{\text{long}} = \sum_{\alpha=p,t,f} T_{zz}^\alpha,$$

$$P_{\text{tr}} = \sum_{\alpha=p,t,f} (T_{xx}^{\alpha} + T_{yy}^{\alpha})/2.$$

Evolution proceeds from the top point of the trajectory downwards. Symbols mark the time intervals along the trajectory. Subtraction of the $m_N n_B$ term is taken for the sake of suitable representation of the plot. The size of the box was chosen to be large enough in order that the amount of matter in it can be representative to conclude on the onset of deconfinement and to be small enough to consider the matter in it as a homogeneous medium. Nevertheless, the matter in the box still amounts to a minor part of the total matter of colliding nuclei. Therefore, only a minor part of the matter of colliding nuclei undergoes the deconfinement transition at 4.9 GeV energy within the 2-phase scenario. As seen, in the 2-phase scenario the deconfinement transition starts at the top AGS energies and gets practically completed at low SPS energies. In the crossover scenario it lasts till very high incident energies.

The 3FD model reproduces the major part of bulk observables, especially within deconfinement scenarios [12, 25–29]. This model does not include viscosity in its formulation. However, dissipation is present through the friction interaction between fluids. This dissipation is strongest at the early stage of the collision, when p- and t-fluids interpenetrate each other. At later stages, the baryon-rich (p- and t-) fluids either get unified or spatially separated. Thus, their friction ceases to act. At the same time the net-baryon-free f-fluid survives as a separate instance till the very freeze-out. At high incident energies ($\sqrt{s_{NN}} \gtrsim 10$ GeV), incomplete baryon stopping results in spatial separation of the projectile-like and target-like leading particles at late stages of the evolution, i.e. a transition from a single baryon-rich cluster of unified p- and t-fluids at lower incident energies to two spatially separated clusters consisting of spatially separated p- and t-fluids at higher energies, takes place. This was illustrated in Ref. [35] for the hadronic scenario. For the deconfinement-transition scenarios the picture is similar. Therefore, at the freeze-out stage the net-baryon-free f-fluid, predominantly located in the center region, is well separated in space from the baryon-rich (p- and t-) ones at $\sqrt{s_{NN}} \gtrsim 10$ GeV. It only overlaps with a small fraction of the unified baryon-rich fluid stopped near midrapidity, the amount of this unified stopped matter gradually decreases with the incident energy rise. Therefore, the dissipation produced by friction between unified baryon-rich fluid consisting of p- and t-ones, and the net-baryon-free f-fluid at the late stage of the collision also gradually decreases with the energy rise. In terms of an effective viscosity of the multi-fluid system it implies that the viscosity also gradually decreases. Though it is highly difficult to quantitatively express the 3FD dissipation in terms of the effective viscosity, because this dissipation depends on the dynamics of the collisions rather than only on the parameters of the 3FD model.

At lower incident energies ($\sqrt{s_{NN}} \lesssim 10$ GeV) the overlap between baryon-rich (p and t) and net-baryon-free

(f) fluids is stronger, however, the density of the f-fluid becomes lower. Therefore, it is not obvious that the dissipation is strong.

Any case, the elliptic flow is the most sensitive quantity to the dissipation effects. Comparison of the 3FD predictions with experimental data on the elliptic flow should indicate how relevant the above mechanism of dissipation is.

The elliptic flow is proportional to the spatial anisotropy [38, 39] usually described by an eccentricity ε defined as

$$\varepsilon = \frac{\langle y^2 \rangle - \langle x^2 \rangle}{\langle y^2 \rangle + \langle x^2 \rangle}, \quad (1)$$

where $\langle x^2 \rangle$ and $\langle y^2 \rangle$ are mean square values of spacial transverse coordinates in and out of the reaction plane, respectively. These mean values are usually calculated with either the wounded-nucleon (WN) or the binary-collision (BC) weights, for details see Ref. [40]. These calculations are based on the usual Woods–Saxon profile of the nuclear density

$$\rho(r) = \frac{\rho_0}{1 + \exp[(r - R_A)/d]}, \quad (2)$$

where ρ_0 is the normal nuclear density, $R_A = 1.12A^{1/3}$ is the radius of a nucleus with a mass number A , and d is a diffuseness of the nuclear surface. As long as the eccentricity is small, elliptic flow should be directly proportional to the eccentricity. For numerically large eccentricities the direct proportionality could break in principle, but as was shown in the very first hydrodynamic calculation by Ollitrault [38] the proportionality holds well even for rather large values of ε .

Within the 3FD model the initial nuclei are represented by sharp-edged spheres, i.e. with zero diffuseness ($d = 0$). This is done for stability of the incident nuclei before collision. However, this approximation essentially affects the eccentricity. The results obtained with $d = 0$ and the realistic value of $d = 0.6$ fm calculated with BC weights are shown in Fig. 2. As seen, the ($d = 0$)-result noticeably exceeds the eccentricity for the realistic value of $d = 0.6$ fm. The ($d = 0.6$ fm)-result with BN weights practically coincides with the eccentricity calculated with WN weights that is accepted as a default eccentricity in the experimental analysis [40]. The overestimation of ε in the 3FD model naturally causes a respective overestimation of the elliptic flow. In order to resolve this problem, the calculated values of v_2 are rescaled with the factor of $\varepsilon_{BN}(d = 0.6 \text{ fm})/\varepsilon_{BN}(d = 0)$. This recipe does not imply that eccentricities calculated within the Glauber model and the 3FD model necessarily coincide. It only assumes that the eccentricities as a function of the surface diffuseness change similarly within the Glauber and 3FD models, more precisely, $\varepsilon_{BN}(d = 0.6 \text{ fm})/\varepsilon_{BN}(d = 0) \approx \varepsilon_{3FD}(d = 0.6 \text{ fm})/\varepsilon_{3FD}(d = 0)$. This assumption is based on the fact that at a fixed impact parameter the eccentricity decreases with diffuseness rise due to simple geometrical reasons which hold true for both models.

In the earlier works on the elliptic flow with the purely hadronic EoS [20–22] this rescaling was not applied, because its need was realized only recently.

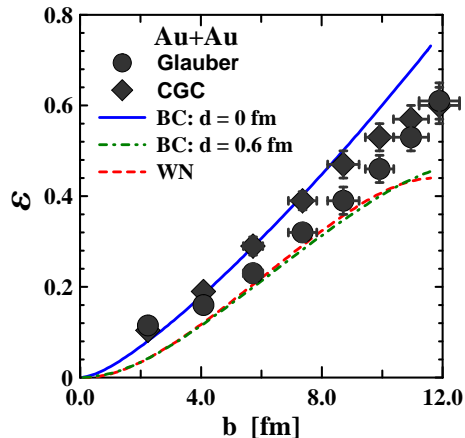


FIG. 2: (Color online) Spatial eccentricity ε as a function of impact parameter in Au+Au collisions for different surface diffusenesses (d) of the Au nucleus and different weights of averaging: the wounded-nucleon (WN) and the binary-collision (BC) weights [40]. The results on $\varepsilon_{\text{part}}\{2\}$ [see Eqs. (3) and (4)] are also displayed. These are calculated in Ref. [1] within the Monte-Carlo Glauber and Color Glass Condensate (CGC) models.

Figure 2 also displays the root-mean-square participant eccentricity, $\varepsilon_{\text{part}}\{2\}$, defined as [1]

$$\varepsilon_{\text{part}} = \frac{\sqrt{(\sigma_y^2 - \sigma_x^2)^2 + 4\sigma_{xy}^2}}{\sigma_y^2 + \sigma_x^2}, \quad \varepsilon_{\text{part}}\{2\} = \sqrt{\langle \varepsilon_{\text{part}}^2 \rangle} \quad (3)$$

$$\sigma_x^2 = \{x^2\} - \{x\}^2, \quad \sigma_y^2 = \{y^2\} - \{y\}^2, \\ \sigma_{xy} = \{xy\} - \{x\}\{y\}, \quad (4)$$

where the curly brackets denote the average over all participants per event, while $\langle \dots \rangle$, the average over events, and x and y are the positions of participant nucleons. Thus defined eccentricity takes into account event-by-event fluctuations with respect to the participant plane caused by a finite number of participant particles. The results displayed in Fig. 2 are calculated in Ref. [1] with the Monte-Carlo Glauber model [41, 42] and the Color Glass Condensate (CGC) model [43–45]. Correspondence between experimental centrality and impact parameter is taken from Ref. [48] where the mean values of the impact parameter were obtained using a Monte-Carlo Glauber calculation.

The displayed results on $\varepsilon_{\text{part}}\{2\}$ demonstrate two points. First, there is an uncertainty related to the rescaling described above. Only for mid-central collisions ($b = 5–9$), $\varepsilon_{BN}(d = 0.6 \text{ fm})$ is close to $\varepsilon_{\text{part}}\{2\}$ (Glauber). At smaller and bigger impact parameters the difference is substantial. Second, possible effects of the fluctuations resulting from a finite number of participant particles

could be significant beyond the range of mid-central collisions. Certainly, such kind of fluctuations are beyond the scope of the 3FD model because it deals only with continuous-medium quantities.

At RHIC and LHC energies the above mentioned Glauber and CGC models are conventionally used to prepare an initial state for the further hydrodynamic treatment of the expanding system. The advantage of thus constructed initial state is that it takes into account random fluctuations. Though, such an initial state is “static”, i.e. the initial collective motion is disregarded. However, an advanced version of the Glauber model [46] overcomes the latter shortcoming, it is able to take into account large accumulated angular momentum and shear flow that affect the directed flow and other odd harmonics of the collective flow [47].

III. INTEGRATED ELLIPTIC FLOW OF CHARGED PARTICLES

Calculations of the integrated elliptic flow of charged particles were performed at fixed impact parameters b which relate to experimental centralities as described above [48]. The integration over transverse momentum (p_t) was cut from above, $p_t < 2 \text{ GeV}/c$. This constraint was chosen because the STAR data were taken with this acceptance. Another reason is that the hydrodynamic treatment becomes inapplicable at high transverse momenta, as claimed in Ref. [57], already at $p_t > 1.5 \text{ GeV}/c$.

Comparison of the integrated elliptic flow of charged particles at midrapidity calculated within different scenarios with STAR data [1] for different centralities is presented in Fig. 3. Only the $v_2\{EP\}$ subset of data is presented because other data subsets are quite indistinguishable from the former one within the scale of this figure. As seen, all different scenarios give almost identical results which perfectly agree with the data for mid-central collisions (centralities 5–30% or $b = 4–6 \text{ fm}$). However, in view of above discussed uncertainties of the eccentricity rescaling and the fact that the STAR data [1] actually correspond to the elliptic flow averaged over pseudorapidity region $|\eta| < 1^4$ this agreement should be considered as simply good.

Again relying on discussion in the previous section, the observed underestimation of the elliptic flow at $b = 2 \text{ fm}$ can be associated with fluctuations resulting from a finite number of participant particles. The calculated v_2 is approximately twice as low as compared with data. The subset $v_2(EP)$ of the STAR data is evaluated versus an event plane, which generally does not coincide with the reaction plane, with respect to which the 3FD v_2 is determined. The difference results from fluctuations,

⁴ see the discussion, concerning Fig. 4, below

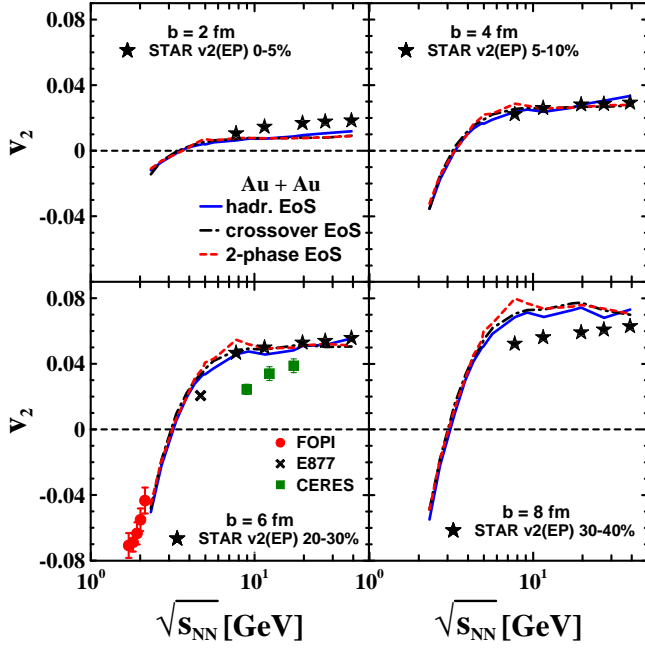


FIG. 3: (Color online) Elliptic flow of charged particles at midrapidity as a function of incident energy in collisions Au+Au at various centralities (impact parameters, b) obtained under the constraint of $p_t < 2$ GeV/c. Experimental data on the integral elliptic flow of charged particles are from STAR Collaboration [1] (subset v2(EP)). FOPI data for $Z=1$ particles [49], as well as E877 [50] and CERES [51] data for charged particles are also displayed.

the effect of which is especially strong in near-central collisions. As seen from Fig. 2, the eccentricity ε_{WN} at $b = 2$ fm calculated without fluctuations is approximately twice as low as compared with $\varepsilon_{\text{part}}[2]$ that takes into account event-by-event fluctuations. In particular, the fluctuations make the event-plane v_2 value non-zero even for head-on collisions, while the non-fluctuating reaction-plane v_2 is identically zero in this case. At more peripheral collisions the fluctuation effect is weaker, as it also seen from Fig. 2, and therefore the applicability of the 3FD (fluctuation-free) model is better. The observed overestimation of the elliptic flow at $b = 8$ fm is expected. At large impact parameters, the number of particles in the participant zone becomes small. Therefore, the applicability of the hydrodynamics becomes worse.

As for the predicted non-monotonicity of the integrated v_2 [3] as a function of $\sqrt{s_{\text{NN}}}$, it indeed takes place for first-order-transition scenario: see a weak pick at $\sqrt{s_{\text{NN}}} \approx 8$ GeV and the subsequent fall. Although, this non-monotonicity is very weak for charged particles. It is not observed in data.

In Fig. 3, FOPI data for $Z=1$ particles [49], as well as E877 [50] and CERES [51] data for charged particles are also displayed. The CERES data appreciably differ from those of the STAR collaboration. Recently there were published new CERES data [52], however, only on differential v_2 . The FOPI data are included because $Z=1$ par-

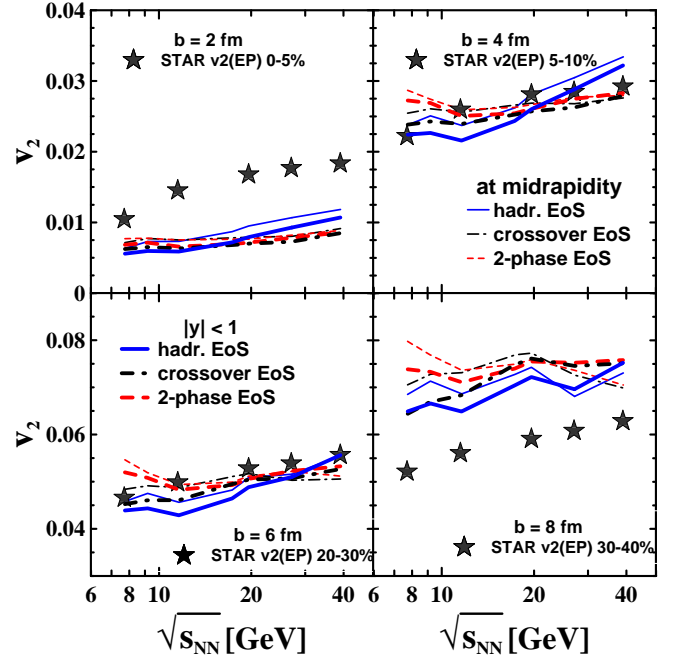


FIG. 4: (Color online) The same as in Fig. 3 but with zoomed regions of the STAR data [1]. In addition to the midrapidity v_2 (thin lines), the elliptic flow averaged over rapidity region $|y| < 1$ is presented (bold lines).

ticles dominate among charged particles in the respective energy range. As seen from Fig. 3, all considered scenarios properly describe the change of sign of the elliptic flow at the incident energy decrease and approach the FOPI data. It is even better seen in Fig. 5, where proton v_2 is presented with additional experimental data. These negative values are a consequence of the squeeze-out effect resulting from blocking of the expanding central blob, consisting of the unified p- and t-fluids⁵, by the spectator matter.

Figure 4 displays zoomed regions of the STAR data [1]. In addition to the midrapidity v_2 of charged particles (thin lines), the elliptic flow of charged particles averaged over a rapidity region $|y| < 1$ is also presented (bold lines):

$$v_2(|y| < 1) = \int_{-1}^1 dy v_2(y) \frac{dN}{dy} / \int_{-1}^1 dy \frac{dN}{dy} \quad (5)$$

where dN/dy is a rapidity distribution of charged particles. This is done because the STAR data [1] in fact correspond to the elliptic flow of charged particles averaged over a pseudorapidity region $|\eta| < 1$. Of course, conditions $|y| < 1$ and $|\eta| < 1$ are not identical. However, the $|y| < 1$ condition is a good approximation to $|\eta| < 1$ at high incident energies, when charged particles are dominated by pions. As seen from Fig. 4, the

⁵ The f-fluid is negligible at these collision energies.

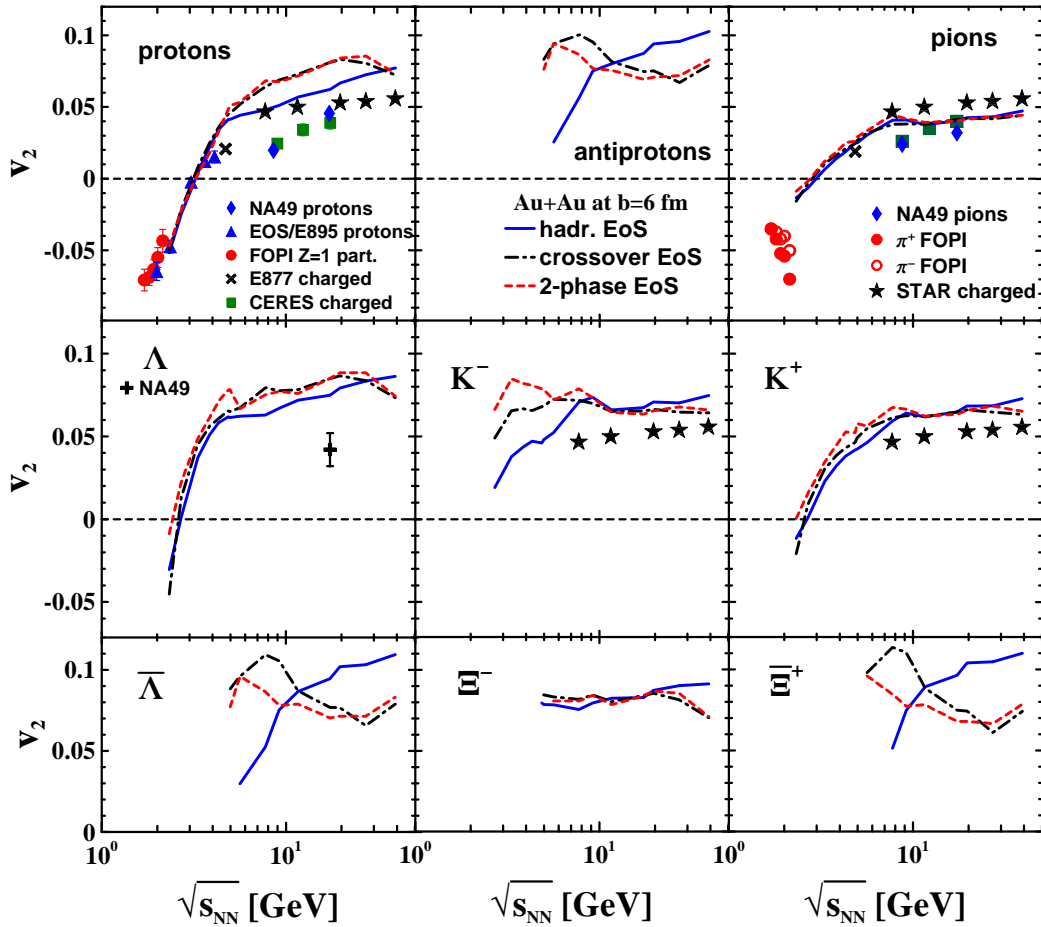


FIG. 5: (Color online) Transverse-momentum integrated elliptic flow of various hadronic species at midrapidity as a function of incident energy in mid-central collisions Au+Au at $b = 6$ fm obtained under constraint $p_t < 2$ GeV/c. Experimental data on the integral elliptic flow are from FOPI Collaboration for Z=1 particles [49], EOS and E895 [53] for protons, E877 [50] and CERES [51] for all charged particles, NA49 for protons [54], pions [54], and Λ hyperons [55], and STAR [1] (subset v2(EP) at 20-30% centrality) for all charged particles. FOPI pion data are from [56].

difference between midrapidity $v_2(y = 0)$ and averaged $v_2(|y| < 1)$ values of the elliptic flow is not large. Moreover, this difference is comparable with the accuracy of computation ($\lesssim 15\%$). This justifies the comparison of the STAR data [1] with the calculated midrapidity v_2 in Fig. 3.

IV. INTEGRATED ELLIPTIC FLOW OF IDENTIFIED HADRONS

Let us turn to the elliptic flow integrated over transverse momentum for various species within different scenarios. Results of such calculations are presented in Figs. 5 for mid-central ($b = 6$ fm) collisions of Au+Au. The integration over transverse momentum (p_t) is again cut from above, $p_t < 2$ GeV/c. Excitation functions of anti-baryons and heavy hyperons are displayed starting from energies above threshold of their production in the nucleon-nucleon collision. Below this threshold the

hydrodynamic treatment of these species is inapplicable because of low multiplicities of these species. The calculated v_2 values have accuracy not worse than 15% (depending on the species and energy), as it was found in computations with finer grid. Results of the simulations computed in Fig. 5 are confronted to available data on the elliptic flow of protons, pions and lambdas. Data on the elliptic flow of charged particles are also displayed to guide an eye.

Here, predictions of alternative scenarios differ from each other to a different extent depending on a particle. As seen from Fig. 5, the energy evolution of the midrapidity v_2 exhibits two basic patterns which also take place in excitation functions of the inverse slopes and mean transverse masses [29]. The first pattern (pattern I) is characteristic of baryons which populate all regions (both central and peripheral) of the excited system. In terms of the 3FD model, they originate predominately from the baryon-rich (p- and t-) fluids. Within this pattern, v_2 rises with energy sometimes beginning from negative

values at low energies. As mentioned above, these negative values result from the squeeze-out effect.

The second pattern (pattern II) is characteristic of anti-baryons which are predominately produced in the central region of the excited system. In terms of the 3FD model, they originate from the net-baryon-free f-fluid. The energy evolution of the anti-baryon v_2 is very distinct in purely hadronic and deconfinement scenarios. This distinction results from difference in dynamical evolution of the f-fluid that have already been discussed in Ref. [29] devoted to analysis of transverse-momentum spectra.

The dynamical evolution of the f-fluid is determined by three factors: a degree of stopping of colliding nuclei (i.e. the friction between them), the formation time (τ) of the f-fluid, and the EoS itself. The friction specifies the initial conditions, i.e. the energy deposit into the f-fluid. The formation time determines the beginning of the hydrodynamical expansion. Before it a collisionless expansion takes place. The EoS controls the character of the hydrodynamical expansion. The first two quantities, the friction and τ , were chosen on the condition of the best reproduction major part of bulk observables for each EoS, see Ref. [25, 27].

The hadronic scenario is characterized by considerably longer formation time ($\tau = 2$ fm/c) and stronger friction as compared to the deconfinement scenarios ($\tau = 0.17$ fm/c). Therefore, in the hadronic scenario the f-fluid exercises a longer collisionless expansion during which the spatial eccentricity of the system drops while the elliptic flow is not formed. The hydrodynamical expansion starts from essentially less deformed configuration as compared with that in the deconfinement scenarios. Thus, the hydrodynamically generated elliptic flow turns out to be lower than in the deconfinement scenarios at $\sqrt{s_{NN}} \lesssim 10$ GeV. At higher energies, two other factors (the friction and EoS) come into game. The energy deposit into the f-fluid turns out to be higher in the hadronic scenario than that for the deconfinement ones, which, in particular, is manifested in overestimation of anti-baryon and, somewhat later, meson production within the hadronic scenario [27]. Besides, the deconfinement EoS's reduce the elliptic flow because they are softer than the hadronic one. As a result, the elliptic flow within the hadronic scenario becomes higher than that in the deconfinement ones.

Mesons demonstrate intermediate (between patterns I and II) behavior depending on whether they predominately produced in the central region or originate from both central and peripheral regions. Mesons, which require lower energy deposit for their production (pions and positive kaons), exhibit the v_2 behavior more similar to that of baryons (pattern I). At the same time, mesons, for production of which a higher energy deposit is needed (negative kaons), predominately originate from highly excited central region and hence their v_2 excitation functions are more similar to that of anti-baryons (pattern II).

As already mentioned, the difference between predictions of the purely hadronic scenario and deconfinement ones is substantial for hadrons exhibiting pattern-II behavior. In particular, in this case the v_2 value indeed exhibits a non-monotonicity within the deconfinement scenarios that was predicted in Ref. [3]. The reason is the same as that discussed in Ref. [12] concerning the difference between the proton and antiproton v_2 . The proton v_2 at midrapidity is formed by particles from both the spatially center and peripheral regions of the nuclear system. This happens because the nuclear stopping is already quite strong at $\sqrt{s_{NN}} \leq 10$ GeV, and hence the midrapidity quantities are determined not only by particles newly produced near the spacial center. The center and peripheral regions differently contribute to the midrapidity elliptic flow of different species, because they have different v_2 patterns. The interference between different v_2 patterns washes out the non-monotonicity inherent in a separate pattern. At the same time, antiprotons are mostly produced from the central region with a definite v_2 pattern that survives in its midrapidity excitation function. This is also applicable to other antibarions and, to a lesser extent, to negative kaons.

However, the multiplicities of anti-baryons are low at $\sqrt{s_{NN}} \leq 10$ GeV. This results in large fluctuations of their v_2 which are, of course, beyond the scope of the 3FD model. This fluctuations can reduce the observable v_2 and thus wash out the non-monotonicity. A possible destructive role of these fluctuations was indicated in Ref. [13]. It was shown that local fluctuations of the baryon number may lead to a biased determination of the event plane which may result in artificial reduction of antiproton v_2 . The same mechanism of reduction is applicable to all other species of low multiplicity. The data on yet differential v_2 of antiprotons recently published by STAR Collaboration [2] apparently testify in favor of such scenario.

V. SUMMARY

The integrated elliptic flow of charged particles from Au+Au collisions was analyzed in a wide range of incident energies $2.7 \text{ GeV} \leq \sqrt{s_{NN}} \leq 39 \text{ GeV}$. The analysis was done within the three-fluid model [18] employing three different EoS's: a purely hadronic EoS [19] and two versions of the EoS involving the deconfinement transition [24]. These are an EoS with a first-order phase transition and that with a smooth crossover transition. It is found that all considered scenarios well reproduce recent STAR data [1] on the integrated elliptic of charged particles for mid-central Au+Au collisions. Moreover, all considered scenarios properly describe the change of sign of the elliptic flow at the incident energy decrease below $\sqrt{s_{NN}} \approx 3.5 \text{ GeV}$. The problems met with central and peripheral collisions are naturally explained by restricted applicability of the 3FD model to those cases.

The present simulations demonstrated that the inte-

grated elliptic flow for charged particles at AGS-SPS-RHIC energies reveals low sensitivity to the EoS in agreement with the same observation made in Ref. [7, 17] for SPS and top RHIC energies. Even within the first-order-transition scenario the calculated elliptic flow of charged particles practically does not exhibit the non-monotonicity of the v_2 as a function of $\sqrt{s_{NN}}$ predicted in [3]. This is a consequence of the nuclear stopping that is already substantial at $\sqrt{s_{NN}} < 10$ GeV. Hence the midrapidity quantities are determined not only by particles newly produced near the spacial center. The center and peripheral regions differently contribute to the midrapidity elliptic flow because they have different v_2 patterns. The interference between different v_2 patterns washes out the non-monotonicity inherent in a separate pattern.

The integrated elliptic flow of various species from Au+Au collisions was also predicted in simulations with the same three EoS's within the same energy range. A noticeable sensitivity to the EoS is found only for anti-baryons and, to a lesser extent, for K^- mesons. In particular, in this case the v_2 excitation function indeed ex-

hibits a non-monotonicity within the deconfinement scenarios that was predicted in Ref. [3]. Anti-baryons (and, to a lesser extent, K^- mesons) are mostly produced in the central region with a definite v_2 pattern and their v_2 pattern is weakly affected by interference with those of peripheral regions. However, the multiplicities of anti-baryons are low at $\sqrt{s_{NN}} \leq 10$ GeV. This results in large fluctuations of their v_2 . The fluctuations can reduce the observable v_2 and thus wash out the non-monotonicity. A possible destructive role of these fluctuations was indicated in Ref. [13]. The data on yet differential v_2 of anti-protons recently published by STAR Collaboration [2] apparently testify in favor of such scenario.

Acknowledgements

We are grateful to A.S. Khvorostukhin, V.V. Skokov, and V.D. Toneev for providing us with the tabulated 2-phase and crossover EoS's. The calculations were performed at the computer cluster of GSI (Darmstadt). This work was partially supported by grant NS-932.2014.2.

-
- [1] L. Adamczyk *et al.* [STAR Collaboration], Phys. Rev. C **86**, 054908 (2012) [arXiv:1206.5528 [nucl-ex]].
 - [2] L. Adamczyk *et al.* [STAR Collaboration], Phys. Rev. C **88** 14902 (2013) [arXiv:1301.2348].
 - [3] P. F. Kolb, J. Sollfrank and U. W. Heinz, Phys. Rev. C **62**, 054909 (2000) [hep-ph/0006129].
 - [4] G. Kestin and U. W. Heinz, Eur. Phys. J. C **61**, 545 (2009) [arXiv:0806.4539 [nucl-th]].
 - [5] J. Auvinen and H. Petersen, Phys. Rev. C **88**, 064908 (2013) [arXiv:1310.1764 [nucl-th]].
 - [6] H. Petersen and M. Bleicher, Phys. Rev. C **79**, 054904 (2009) [arXiv:0901.3821 [nucl-th]].
 - [7] H. Petersen and M. Bleicher, Phys. Rev. C **81**, 044906 (2010) [arXiv:1002.1003 [nucl-th]].
 - [8] V. P. Konchakovski, E. L. Bratkovskaya, W. Cassing, V. D. Toneev, S. A. Voloshin and V. Voronyuk, Phys. Rev. C **85**, 044922 (2012) [arXiv:1201.3320 [nucl-th]].
 - [9] C. Shen and U. Heinz, Phys. Rev. C **85**, 054902 (2012) [Erratum-ibid. C **86**, 049903 (2012)] [arXiv:1202.6620 [nucl-th]].
 - [10] D. Solanki, P. Sorensen, S. Basu, R. Raniwala and T. K. Nayak, Phys. Lett. B **720**, 352 (2013) [arXiv:1210.0512 [nucl-ex]].
 - [11] S. Plumari, V. Greco and L. P. Csernai, arXiv:1304.6566 [nucl-th].
 - [12] Yu. B. Ivanov, Phys. Lett. B **723**, 475 (2013) [arXiv:1304.2307 [nucl-th]].
 - [13] J. Steinheimer, V. Koch and M. Bleicher, Phys. Rev. C **86**, 044903 (2012) [arXiv:1207.2791 [nucl-th]].
 - [14] G. S. Denicol, C. Gale, S. Jeon and J. Noronha, Phys. Rev. C **88**, no. 6, 064901 (2013) [arXiv:1308.1923 [nucl-th]].
 - [15] A. S. Khvorostukhin, V. D. Toneev and D. N. Voskresensky, Nucl. Phys. A **845**, 106 (2010) [arXiv:1003.3531 [nucl-th]].
 - [16] R. A. Lacey, A. Taranenko, J. Jia, D. Reynolds, N. N. Ajitanand, J. M. Alexander, Y. Gu and A. Mwai, Phys. Rev. Lett. **112**, 082302 (2014) [arXiv:1305.3341 [nucl-ex]].
 - [17] D. M. Dudek, W. L. Qian, C. Wu, O. Socolowski, S. S. Padula, G. Krein, Y. Hama and T. Kodama, arXiv:1409.0278 [nucl-th].
 - [18] Yu. B. Ivanov, V. N. Russkikh, and V.D. Toneev, Phys. Rev. C **73**, 044904 (2006) [nucl-th/0503088].
 - [19] V. M. Galitsky and I. N. Mishustin, Sov. J. Nucl. Phys. **29**, 181 (1979).
 - [20] V. N. Russkikh and Yu. B. Ivanov, Phys. Rev. C **74** (2006) 034904 [nucl-th/0606007].
 - [21] Yu. B. Ivanov and V. N. Russkikh, PoS CPOD **07**, 008 (2007) [arXiv:0710.3708 [nucl-th]].
 - [22] Yu. B. Ivanov, I. N. Mishustin, V. N. Russkikh, and L. M. Satarov, Phys. Rev. C **80**, 064904 (2009) [arXiv:0907.4140 [nucl-th]].
 - [23] L. P. Csernai, D. D. Strottman and C. Anderlik, Phys. Rev. C **85**, 054901 (2012) [arXiv:1112.4287 [nucl-th]].
 - [24] A. S. Khvorostukhin, V. V. Skokov, K. Redlich, and V. D. Toneev, Eur. Phys. J. **C48**, 531 (2006) [nucl-th/0605069].
 - [25] Yu. B. Ivanov, Phys. Rev. C **87**, 064904 (2013) [arXiv:1302.5766 [nucl-th]].
 - [26] Yu. B. Ivanov, Phys. Lett. B **721**, 123 (2013) [arXiv:1211.2579 [hep-ph]].
 - [27] Yu. B. Ivanov, Phys. Rev. C **87**, 064905 (2013) [arXiv:1304.1638 [nucl-th]].
 - [28] Yu. B. Ivanov, Phys. Lett. B **726**, 422 (2013) [arXiv:1306.0994 [nucl-th]].
 - [29] Yu. B. Ivanov, Phys. Rev. C **89**, 024903 (2014) [arXiv:1311.0109 [nucl-th]].
 - [30] U. Katscher, D.H. Rischke, J.A. Maruhn, W. Greiner, I.N. Mishustin, and L.M. Satarov, Z. Phys. **A346**, 209 (1993); A. Dumitru, U. Katscher, J.A. Maruhn, H. Stöcker, W. Greiner, and D.H. Rischke, Phys. Rev. C

- 51**, 2166 (1995) [hep-ph/9411358]; Z. Phys. **A353**, 187 (1995) [hep-ph/9503347].
- [31] J. Brachmann, A. Dumitru, J.A. Maruhn, H. Stöcker, W. Greiner, and D.H. Rischke, Nucl. Phys. **A619**, 391 (1997) [nucl-th/9703032]; M. Reiter, A. Dumitru, J. Brachmann, J.A. Maruhn, H. Stöcker, and W. Greiner, Nucl. Phys. **A643**, 99 (1998) [nucl-th/9806010]; M. Bleicher, M. Reiter, A. Dumitru, J. Brachmann, C. Spieles, S.A. Bass, H. Stöcker, and W. Greiner, Phys. Rev. C **59**, R1844 (1999) [hep-ph/9811459].
- [32] S. Bass, *et al.*, Prog. Part. Nucl. Phys. **41**, 225 (1998) [nucl-th/9803035].
- [33] W. Cassing and E. L. Bratkovskaya, Phys. Rept. **308**, 65 (1999).
- [34] W. Cassing, E. L. Bratkovskaya, Nucl. Phys. A **831**, 215 (2009) [arXiv:0907.5331 [nucl-th]]; Phys. Rev. C **78**, 034919 (2008) [arXiv:0808.0022 [hep-ph]]; W. Cassing, Nucl. Phys. A **791**, 365 (2007) [arXiv:0704.1410 [nucl-th]].
- [35] V. N. Russkikh and Yu. B. Ivanov, Phys. Rev. C **76**, 054907 (2007) [nucl-th/0611094].
- [36] Yu. B. Ivanov and V. N. Russkikh, Phys. Atom. Nucl. **72**, 1238 (2009) [arXiv:0810.2262 [nucl-th]].
- [37] I. C. Arsene, L.V. Bravina, W. Cassing, Yu.B. Ivanov, A. Larionov, J. Randrup, V.N. Russkikh, V.D. Toneev, G. Zeeb, D. Zschesche, Phys. Rev. C **75**, 034902 (2007) [nucl-th/0609042].
- [38] J. -Y. Ollitrault, Phys. Rev. D **46**, 229 (1992).
- [39] S. A. Voloshin, A. M. Poskanzer and R. Snellings, Elementary Particles, Nuclei and Atoms (Springer-Verlag) **23**, 293 (2010) [arXiv:0809.2949 [nucl-ex]].
- [40] P. Jacobs and G. Cooper, arXiv:nucl-ex/0008015.
- [41] M. Miller and R. Snellings, nucl-ex/0312008.
- [42] M. L. Miller, K. Reygers, S. J. Sanders and P. Steinberg, Ann. Rev. Nucl. Part. Sci. **57**, 205 (2007) [nucl-ex/0701025].
- [43] H. -J. Drescher, A. Dumitru, A. Hayashigaki and Y. Nara, Phys. Rev. C **74**, 044905 (2006) [nucl-th/0605012].
- [44] H. -J. Drescher and Y. Nara, Phys. Rev. C **75**, 034905 (2007) [nucl-th/0611017]; *ibid.* **76**, 041903 (2007) [arXiv:0707.0249 [nucl-th]].
- [45] T. Hirano and Y. Nara, Phys. Rev. C **79**, 064904 (2009) [arXiv:0904.4080 [nucl-th]].
- [46] V. Vovchenko, D. Anchishkin and L. P. Csernai, Phys. Rev. C **90**, no. 4, 044907 (2014) [arXiv:1407.4644 [nucl-th]].
- [47] L. P. Csernai and H. Stoecker, J. Phys. G **41**, no. 12, 124001 (2014) arXiv:1406.1153 [nucl-th].
- [48] J. Adams *et al.* [STAR Collaboration], Phys. Rev. C **73**, 034903 (2006) [nucl-ex/0510053].
- [49] A. Andronic *et al.* (FOPI Collaboration), Phys. Lett. **B612**, 173 (2005) [arXiv:nucl-ex/0411024].
- [50] P. Braun-Munzinger and J. Stachel, Nucl. Phys. A **638**, 3 (1998) [nucl-ex/9803015].
- [51] D. Adamova *et al.* [CERES Collaboration], Nucl. Phys. A **698**, 253 (2002).
- [52] D. Adamova *et al.* [CERES Collaboration], Nucl. Phys. A **894**, 41 (2012) [arXiv:1205.3692 [nucl-ex]].
- [53] C. Pinkenburg *et al.* [E895 Collaboration], Phys. Rev. Lett. **83**, 1295 (1999) [nucl-ex/9903010].
- [54] C. Alt *et al.* [NA49 Collaboration], Phys. Rev. C **68**, 034903 (2003) [nucl-ex/0303001].
- [55] C. Alt *et al.* [NA49 Collaboration], Phys. Rev. C **75**, 044901 (2007) [nucl-ex/0606026].
- [56] W. Reisdorf, *et al.* (FOPI Collaboration), Nucl. Phys. **A781**, 459 (2007) [arXiv:nucl-ex/0610025].
- [57] U. W. Heinz, in 'Relativistic Heavy Ion Physics', Landolt-Boernstein New Series, I/23, edited by R. Stock (Springer Verlag, New York, 2010) Chap. 5 [arXiv:0901.4355 [nucl-th]].